Available online at www.sciencedirect.com
SCIENCE DIRECT
Acta Materialia 54 (2006) 1863–1876
Acta MATERIALIA
www.actamat-journals.com

Three-dimensional investigation of the texture and microstructure below a nanoindent in a Cu single crystal using 3D EBSD and crystal plasticity finite element simulations

N. Zaafarani [a], D. Raabe [a,*], R.N. Singh [b], F. Roters [a], S. Zaefferer [a]

[a] *Max-Planck-Institut für Eisenforschung, Abteilung Mikrostrukturphysik und Umformtechnik, Max-Planck-Strasse 1, 40237 Düsseldorf, Germany*
[b] *Mechanical Metallurgy Section, Materials Science Division, Bhabha Atomic Research Centre, Trombay, Mumbai 400 085, India*

Received 15 October 2005; received in revised form 6 December 2005; accepted 8 December 2005
Available online 17 February 2006

Abstract

This paper reports a three-dimensional (3D) study of the microstructure and texture below a conical nanoindent in a (1 1 1) Cu single crystal at nanometer-scale resolution. The experiments are conducted using a joint high-resolution field emission scanning electron microscopy/electron backscatter diffraction (EBSD) set-up coupled with serial sectioning in a focused ion beam system in the form of a cross-beam 3D crystal orientation microscope (3D EBSD). The experiments (conducted in sets of subsequent $(1\,1\,\bar{2})$ cross-section planes) reveal a pronounced deformation-induced 3D patterning of the lattice rotations below the indent. In the cross-section planes perpendicular to the (1 1 1) surface plane below the indenter tip the observed deformation-induced rotation pattern is characterized by an outer tangent zone with large absolute values of the rotations and an inner zone closer to the indenter axis with small rotations. The mapping of the rotation directions reveals multiple transition regimes with steep orientation gradients and frequent changes in sign. The experiments are compared to 3D elastic–viscoplastic crystal plasticity finite element simulations adopting the geometry and boundary conditions of the experiments. The simulations show a similar pattern for the absolute orientation changes but they fail to predict the fine details of the patterning of the rotation directions with the frequent changes in sign observed in the experiment. Also the simulations overemphasize the magnitude of the rotation field tangent to the indenter relative to that directly below the indenter tip.

Keywords: 3D EBSD; Focused ion beam; Texture; Nanoindentation; Copper

1. Introduction and motivation

Nanoindentation is a well-established test method for the determination of mechanical properties at microstructural scales [1–3]. The mechanically relevant volume probed by this test typically lies between $(30\,\text{nm})^3$ and $(10\,\mu\text{m})^3$ depending on the indentation set-up and the material indented. Owing to its high lateral resolution, small-scale indentation is not only very useful for determining the mechanical heterogeneity of complex microstructures but also for investigating the local mechanical response of modern miniaturized electronic and engineering devices, micro-electromechanical systems (MEMS), and functional coatings [3].

Due to its complexity, small-scale indentation testing challenges modelers and experimentalists to better understand the deformation mechanisms that govern the mechanics in the indentation zone. The complexity of such tests arises from the complicated boundary and kinematic conditions, microstructural size effects, anisotropy, and heterogeneity of the deformation and stress fields as well as from the corresponding dislocation arrangements that are created below and around an indent [3–12].

There are two main benefits from an improved understanding of nanoindentation. First, the material parameters, which are commonly extracted from the force–displacement curves, could be placed on a more solid theoretical ground.

* Corresponding author. Tel.: +49 211 6792 333.
E-mail address: raabe@mpie.de (D. Raabe).

1359-6454/$30.00
doi:10.1016/j.actamat.2005.12.014

This applies in particular to the field of plasticity where a more detailed comprehension of the contact area, rate and relaxation effects, three-dimensional (3D) stress state, nanoscale friction, and material anisotropy might render the data acquisition more detailed and robust. Second, an enhanced understanding of indentation mechanics might enable one to extract and address a larger spectrum of constitutive material parameters than before. For instance it is conceivable to obtain tensorial rather than only scalar data, precise nanofriction coefficients, residual stresses, flow anisotropy, or small-scale damage effects from nanoindentations at a more quantitative scale than currently possible.

In that context this study addresses, as one particular aspect of nanoindentation, the formation of the crystallographic texture and microstructure in the deformation zone around an indent in three dimensions. For this purpose we use for the first time a novel experimental approach, namely a 3D electron backscatter diffraction (EBSD) texture and microstructure analysis. For this experiment we use a cross-beam microscope, which is a set-up of a high-resolution field emission scanning electron microscopy (SEM) instrument in conjunction with an EBSD system and a focused ion beam (FIB) microscope used for serial sectioning [13–15]. This technique allows us to map the deformation-induced lattice rotations below an indent in three dimensions. The experiment is conducted on a [1 1 1] Cu single crystal with a conical indenter using a Hysitron TriboIndenter set-up. A conical shape is used to avoid symmetries other than those of the crystal structure. The joint investigation of plastic deformation and induced lattice rotations is of great interest for an improved micromechanical understanding of indentation experiments owing to the close connection between crystallographic shear and the resulting lattice spin (the term "lattice spin" is in the following used synonymously for related terms such as crystalline reorientation, texture evolution, or induced lattice rotation).

The experimental 3D observations are compared to corresponding 3D elastic–viscoplastic crystal plasticity finite element simulations which adopt the geometry and boundary conditions of the experiments. The crystal plasticity finite element simulations are essential for the interpretation of the observed rotation fields. They allow us not only to establish the relationship between crystallographic shear and texture but also provide information about the spatial 3D distribution of the individual shear rates on the active slip systems that entail the observed lattice rotations. The latter aspect is of particular interest because the 3D distribution of the shear rate contributions of the 12 slip systems cannot currently be obtained by any other experimental or theoretical method owing to the heterogeneity of the indentation test.

To understand which contributions of the observed deformation and rotation pattern are due to isotropic mechanics as opposed to those effects that have an anisotropic crystallographic background, we also conduct simulations with a J2 yield stress criterion (where J2 is the second invariant of the stress deviator as an isotropic yield criterion). This combination of isotropic and anisotropic (crystal plasticity) finite element simulations enables one to separate carefully macromechanical isotropic effects in the pattern formation from crystallographic aspects [16,17]. This approach has been successfully used before for the interpretation of crystallographic versus isotropic micromechanical aspects in the field of crystal plasticity [18,19].

2. Previous studies on deformation-induced lattice rotations during indentation

Only a few experimental studies have addressed the relationship between indentation and deformation-induced lattice rotations in the vicinity of an indent. In a set of recent papers the group of Larson et al. [20–24] obtained impressive results on the microstructure evolution below indents by using a non-destructive 3D synchrotron diffraction method. In their work they observed a systematic deformation-induced orientation pattern below [1 1 1] indents in Cu single crystals. The experimentally observed pattern was characterized by outward rotations at the rim of the indent (tangent zone of the indent) and inward rotations directly below the indent close to the indenter axis. The results were discussed in terms of Kröner's concept of geometrically necessary dislocations. Wang et al. [25] investigated the dependence of nanoindentation pile-up patterns and of lattice rotations for Cu single crystals with different orientations ([1 0 0], [1 1 0], and [1 1 1]) using a conical indenter. The 2D orientation measurements in this work were conducted around the indents at the surface with a high-resolution EBSD technique but no 3D analysis could be performed at that time.

Previous continuum-based indentation simulations aimed at elucidating the heterogeneity of the mechanics involved in such tests have been published by various groups. Most of these works, however, did not address the formation of crystallographic textures.

Besides the experiments mentioned above, Wang et al. [25] also conducted corresponding simulations using a 3D elastic–viscoplastic crystal plasticity finite element method. The group of Curtin [26,27] used coupled atomistic-continuum modeling for the investigation of nanoindentation. Smith et al. [28] conducted simulations of nanoindentation using an extended version of the quasicontinuum model, which works by embedding an interatomic force law within a finite element framework. Bolshakov and Pharr [29] have investigated the influence of material pile-up on the measurement of mechanical properties by load- and depth-sensing indentation techniques using finite element simulations of conical indentation. Fivel et al. [30] conducted 3D simulations of indent-induced plastic zones at the mesoscale using a combination of 3D discrete dislocation simulation and the finite element method. Durst et al. [31] conducted finite element simulations of spherical indentations in the elastic–plastic transition

regime. In their work they examined spherical indentations using various elastic–perfectly plastic constitutive material laws. Similar work was published by Park and Pharr [32] who investigated nanoindentation with spherical indenters by use of finite element simulations with particular reference to the elastic–plastic transition regime. Lichinchi et al. [33] conducted finite element simulations of nanoindentation of thin films. They applied the method to the investigation of the stress–strain field of thin hard coatings subjected to nanoindentation. Durst et al. [34] conducted finite element simulations of the indentation size effect in metallic materials introducing a correction for the size of the plastic zone. In another work, Durst et al. [35] published a finite element study of nanoindentation measurements on two-phase elastic–plastic materials. In this study, they used the approach to investigate the influence of the shape and the aspect ratio of particles embedded in a matrix material on the deformation behavior and hardness during depth-sensing indentation.

Very detailed atomistic simulations of the incipient stages of nanoindentation in face-centered cubic (fcc) single crystals were recently conducted by Li et al. [36] and Van Vliet et al. [37]. These studies provided excellent insights into the early stages of nucleation of slip during the beginning of indentation. The data revealed a strong influence of the crystallography on the formation of surface patterns.

3. Experimental

3.1. Material and sample preparation

A copper single crystal with a (1 1 1)-oriented surface plane was drawn from the melt and cut into a cube-shaped specimen by spark erosion. The surface plane was wet ground, diamond polished, and finally electropolished. An array of indents was placed on the (1 1 1) plane of the single crystal at a distance of 50 μm from the edge. After indentation the crystal was diamond polished along the $(1\,1\,\bar{2})$ plane using a particle size of 1 μm in order to remove about 20 μm of material perpendicular to the indented (1 1 1) surface (Fig. 1). After polishing, the sample was cleaned in an ultrasonic acetone bath for 5 min. After that pure water and high-pressure air were used to clean the sample of the acetone. The serial sectioning procedure required for the 3D EBSD analysis was directly conducted in the Zeiss joint high-resolution field emission cross-beam 3D SEM/EBSD microscope by the FIB unit (Fig. 2).

3.2. Hardness testing

The nanohardness tests were performed using a Hysitron nanoindenter system (TriboIndenter). The instrument included an *XYZ* sample stage and a set-up combining a piezo-scanner as known from conventional atomic force microscopy (AFM) with a transducer and a conical diamond indenter tip. The *XYZ* stage was used for the fine positioning of the sample under the piezo-scanner and for the approach of the indenter.

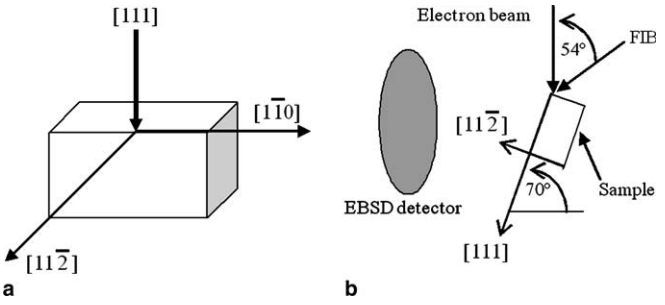

Fig. 1. Schematic showing (a) the crystal directions and (b) the arrangement of the incident secondary electron beam, the specimen, the FIB, and the EBSD detectors. Indents were made into the crystallographic (1 1 1) plane whereas serial sectioning was performed along the $[1\,1\,\bar{2}]$ crystallographic direction (details in Fig. 2).

The experiments were carried out with a conical indenter in order to avoid symmetries other than those of the crystal structure. The nanohardness tests were conducted in load-controlled mode. A triangular loading–unloading pattern was used with a maximum peak load of 10 mN but without any holding time at that load. Loading and unloading were conducted at the same rate of 1.82 mN/s. The displacement of the indenter was measured simultaneously to give a force–displacement curve. To calculate both hardness and Young's modulus accurately from the force–displacement data, it was necessary to know the exact geometry of the indenter tip. Since the depth of penetration in the copper single crystals was too large to be achieved in quartz, the indenter cross-sectional area function was determined by performing indentation tests at different depths on an alternative material with a known and constant Young's modulus (poly(methyl methacrylate)). Some 36 indentation tests in the form of a 6×6 matrix with a spacing of 20 μm between the indents and an indentation depth of about 900 nm were performed, and both hardness and Young's modulus were calculated for each of them. The surface profiles of the indented and surrounding area were determined using AFM.

3.3. Serial sectioning by FIB and 3D EBSD measurements

Our current approach to 3D EBSD was inspired by the work of Uchic et al. [13] and Zaefferer et al. [14,15] as well as by the 3D texture measurements via synchrotron radiation published by the group of Larson [20–24].

The 3D EBSD experiments were conducted using a joint high-resolution field emission SEM/EBSD set-up together with a FIB system in the form of a Zeiss cross-beam 3D crystal orientation microscope. SEM allows for the observation with SE, backscattered electrons, scanning transmission electron microscopy, EBSD, and energy dispersive X-ray analysis. The integrated scanning Ga^+ FIB device allows for the observation with ion-induced SE as well as for sputtering (milling) for serial sectioning, transmission electron microscopy thin-foil preparation, surface

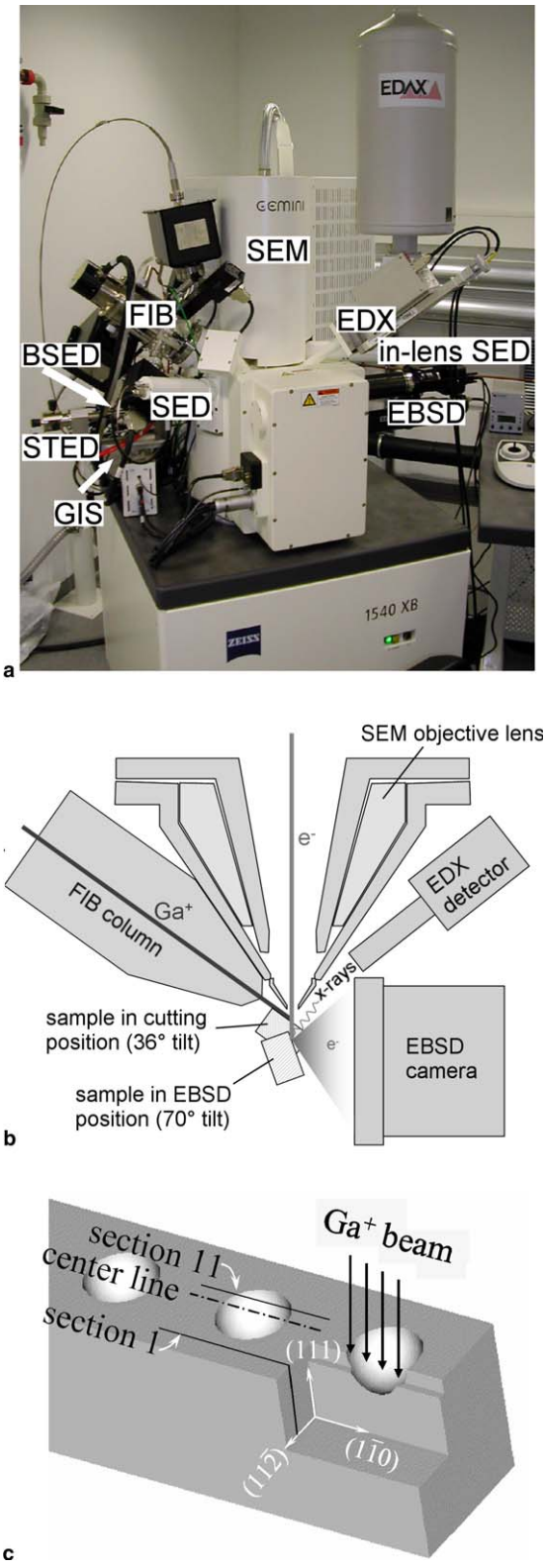

Fig. 2. (a) Joint high-resolution field emission SEM/EBSD set-up together with a FIB system in the form of a cross-beam 3D crystal orientation microscope for conducting 3D EBSD measurements by serial sectioning (Zeiss) [14,15]. (b) Schematic of the joint FIB/EBSD set-up. (c) Schematic of the FIB sectioning geometry. The exact positions of the sections where EBSD mappings were taken are given in Table 1.

structuring, and the deposition of various types of films (W, Pt, SiO_2) from organic precursor gasses.

The particular analysis method chosen in this study involved conducting highly precise and fully automated serial sectioning with the FIB and subsequently mapping the texture in each of those layers using high-resolution EBSD. This approach requires a quick and precise change between milling for serial sectioning (sample at 36°) and EBSD mapping (sample at 70°) (Fig. 2). The minimum possible spatial resolution of the 3D pixels amounts to about $50 \times 50 \times 50$ nm^3 [14,15]. The ion beam did not create noticeable damage, i.e., no serious deterioration of the EBSD pattern quality was observed after milling the copper single crystal. In order to provide protection of the free edges against diffuse FIB cutting, a tungsten layer about 1 μm thick was deposited on the surface over the indent before starting the milling process.

In total a volume of 20 μm along the $[1\,1\,\bar{2}]$, 30 μm along the $[1\,\bar{1}\,0]$, and 20 μm along the $[1\,1\,1]$ direction was removed by FIB serial sectioning in front of the indent to expose gradually the volume inspected. The incident angle of the FIB was normal to the $(1\,1\,1)$ plane and an ion beam current of 500 pA was used for removing the material. For the last milling step before the EBSD characterization a smaller beam current of only 100 pA was used in order to obtain less roughness and better Kikuchi pattern quality. After this final FIB polishing step the sample was tilted to the standard EBSD measurement position. The electron beam had an angle of 20° relative to the $[1\,1\,1]$ direction on the $(1\,1\,\bar{2})$ crystal plane. The EBSD measurements were carried out in each layer after serial sectioning at a step size of 80 nm. The whole process of alternating FIB sectioning and EBSD measurements was carried out for a set of 11 subsequent layers through the 3D deformation zone around the indent.

Table 1 shows that a set of subsequent serial sections were placed near the center plane below the actual indenter tip. For each of those planes EBSD mappings were obtained. The texture data were analyzed in terms of the misorientation angle with respect to the undeformed crystal, of the sense of the crystallographic re-rotation and the axis of rotation.

Table 1
Distance of serial sections from the center plane below the indent

Serial section plane number	Distance from center plane below the indent (μm)	Serial section plane number	Distance from center plane below the indent (μm)
1	7.22	2	5.97
3	5.24	4	1.57
5	0.876	6	0.796
7	0.641	8	0.474
9	0.318	10	0.176
11	−0.484		

4. Simulation of Cu single-crystal indentation

4.1. Introduction

Nanoindentation experiments require careful control of a set of boundary conditions, such as the surface finish, defect-free subsurface of the sample indented, accuracy of the indenter surface and shape, and precise data acquisition. These difficult experimental conditions suggest the use of a finite element approach for simulating indentation. This allows one to investigate the evolution of the material characteristics during the entire indentation process and assign the material data obtained to a specific stress–strain state of the experiment at each instant. In addition it allows one to investigate the sample interior and to modify systematically material or process parameters for conducting numerical experiments.

4.2. Constitutive model

4.2.1. Flow rule

In order to describe the flow kinematics, the finite deformation defined by the deformation gradient F is multiplicatively decomposed into two contributions, namely the elastic part of the deformation gradient F_e and the plastic part of the deformation gradient F_p. The latter quantity describes an intermediate configuration accounting only for the deformation induced by the plastic slip in the lattice, i.e., $\det|F_p| = 1$. F_e captures both the stretch and the rotation of the lattice. The flow rule is used in the form

$$\dot{F}_p = L_p F_p \tag{1}$$

where the plastic velocity gradient L_p is given by

$$L_p = \sum_\alpha \dot{\gamma}_\alpha \left(m_0^\alpha \otimes n_0^\alpha\right) \tag{2}$$

in which m_0^α and n_0^α are the orthonormal vectors describing the slip direction and the slip plane normal of the slip systems α in the reference configuration, respectively, and $\dot{\gamma}_\alpha$ describes the shear rates on the slip systems α.

4.2.2. Hardening mechanism

The material law is based on a crystal plasticity model introduced by Kalidindi et al. [38,39] for the prediction of crystallographic texture based on the phenomenology of the fcc lattice. The hardening law on a slip system α follows:

$$\dot{\gamma}_\alpha = \dot{\gamma}_0 \left|\frac{\tau_\alpha}{s_\alpha}\right|^{1/m} \operatorname{sign}(\tau_\alpha) \tag{3}$$

where $\dot{\gamma}_\alpha$ is the shear rate on the slip system subjected to the resolved shear stress τ_α having a slip resistance of s_α. $\dot{\gamma}_0$ and m are material parameters and are the reference shear rate and the rate sensitivity of slip. The influence of any other slip system β on the hardening behavior of system α is given by

$$\dot{s}_\alpha = \sum_\beta h_{\alpha\beta} \left|\dot{\gamma}_\beta\right| \tag{4}$$

where

$$h_{\alpha\beta} = q_{\alpha\beta}\left[h_0\left(1 - \frac{s_\beta}{s_s}\right)^a\right] \tag{5}$$

In this formulation h_0, a, and s_s are slip hardening parameters, which are assumed to be identical for all fcc slip systems owing to the underlying characteristic dislocation reactions [38,39]. The parameter $q_{\alpha\beta}$ is taken as 1.0 for coplanar slip systems α and β and 1.4 otherwise. The time integration procedure for updating the stresses at the intermediate configuration at time $T = (t + \Delta t)$ is represented by

$$\sigma^*(T) = \sigma^*[s_\alpha(T), F(T), F_p(t)] \tag{6}$$

$$s_\alpha(T) = s_\alpha[s_\alpha(t), s_\beta(T), \sigma^*(T)] \tag{7}$$

which are solved iteratively. The Cauchy stress σ can be determined by

$$\sigma = \frac{1}{\det|F_e|} F_e \sigma^* F_e^T \tag{8}$$

4.2.3. Determination of the constitutive parameters

A compression test for a Cu single crystal was performed in order to determine the values for the material parameters required for the model. Loading was along the [1 1 1] axis, which results in six active slip systems with the same Schmid factor of 0.2722 (Table 2).

The sample used for the compression test was a wire-cut cylinder with dimensions of 3 mm × 4.5 mm (diameter × length). The compression speed was 0.1 mm/s resulting in an average overall strain rate of $4.3 \times 10^{-4}\ s^{-1}$. The strain rate could then be resolved in the shear rate over each activation plane by

$$\dot{\gamma}_\alpha = \frac{\bar{\dot{\varepsilon}}}{6 \times S_{\text{Schmid}}} \tag{9}$$

By fitting the material parameters in the model excellent correspondence could be achieved with the experimental results (Fig. 3). The resulting constitutive material parameters are $h_0 = 200$ MPa, $a = 1$, $s_s = 75$ MPa, $m = 0.012$. The initial value of the slip resistance was chosen as 8 MPa and $\dot{\gamma}_0$ was taken to be $0.001\ s^{-1}$. The elastic constants were those for pure Cu, i.e., $C_{11} = 168$ GPa, $C_{12} = 121.4$ GPa, $C_{44} = 75.4$ GPa.

4.2.4. Finite element model

The constitutive model with the time integration procedure outlined above was implemented in the finite element code MARC using the user-defined subroutine HYPELA2 for the simulation of the indentation of the Cu single crystal [40]. The mesh consisted of 1888 elements (3D quadrilateral, 8 integration points) and 2205 nodes (Fig. 4). Near the center of the model special care was taken when designing the mesh owing to the possibility of high element distortion. Because of the large difference in the elastic stiffness of the diamond indenter and the Cu sample (10:1) the indenter was assumed rigid. As a boundary condition the lower face of the modeled cylinder was kept restricted from any degree

Table 2
Active planes for a Cu single-crystal compression with [1 1 1] loading axis

Plane	(1 1 1)			$(\bar{1}\,1\,1)$			$(1\,\bar{1}\,1)$			$(\bar{1}\,\bar{1}\,1)$		
System	A1	A2	A3	B1	B2	B3	C1	C2	C3	D1	D2	D3
Direction	$0\,1\,\bar{1}$	$\bar{1}\,0\,1$	$1\,\bar{1}\,0$	$0\,1\,\bar{1}$	$1\,0\,1$	$\bar{1}\,\bar{1}\,0$	$0\,\bar{1}\,\bar{1}$	$\bar{1}\,0\,1$	$1\,1\,0$	$0\,\bar{1}\,\bar{1}$	$1\,0\,1$	$\bar{1}\,1\,0$
Schmid factor	0	0	0	0	0.2722	0.2722	0.2722	0	0.2722	0.2722	0.2722	0

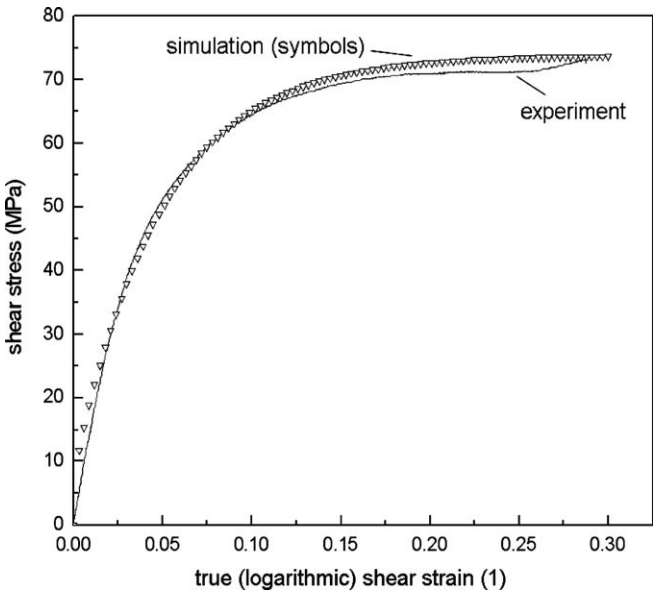

Fig. 3. Stress–strain curve for a shear test obtained from experiment and model fit. The material parameters for the fitting procedure were $h_0 = 200$ MPa, $a = 1$, $s_s = 75$ MPa, $m = 0.012$, an initial value of slip resistance s_0 of 8 MPa, and $\dot{\gamma}_0 = 0.001\ s^{-1}$ (see details in Eqs. (1)–(7)).

of freedom. All other nodes were free to move in any direction. Zero friction was assumed between indenter and sample. The initial orientation of the sample was chosen by selecting appropriate Euler angles such that the x, y, z coordinate system represents the $[1\,\bar{1}\,0]$, $[1\,1\,\bar{2}]$, and $[1\,1\,1]$ crystal directions, respectively.

5. Results and discussion

Fig. 5 shows a micrograph of the indented matrix (Fig. 5(a)) and a close-up of one of the indents (Fig. 5(b)). Fig. 5(c) shows the sixfold symmetry of the pile-up pattern around the (1 1 1) indent, which was earlier observed by Wang et al. [25]. Fig. 6 shows SEM images of two different serial sections along the $[1\,1\,\bar{2}]$ crystal direction, one before the actual indent (Fig. 6(a)) and the other close to the indenter tip (Fig. 6(b)). The micrographs also show the protective tungsten layer that was deposited before the FIB milling process in order to prevent the erosion of the surface edge. The micrographs reveal that a substantial amount of material had to be removed by milling in order to avoid shadowing effects during the subsequent EBSD measurements. From a series of tests we observed that the optimum milling geometry had to follow a trapezoidal shape (Fig. 6(a)).

Fig. 7 shows sets of successive $(1\,1\,\bar{2})$ serial sections perpendicular to the (1 1 1) indentation plane. The sections were taken at different spacings from the actual indenter tip (for geometrical details see Figs. 1 and 2). Scan 4 is far away from the indenter tip (1567 nm) and scan 10 is close to the indenter tip (176 nm) (Table 1). The color code indicates the magnitude of the orientation change relative to the initial undeformed crystal orientation. The color scheme and scaling is identical for all diagrams. The images on the left-hand side (Fig. 7(a)–(h)) were obtained from crystal plasticity finite element simulations as outlined above. The corresponding misorientation maps on the right-hand side were determined via EBSD measurements in each layer prepared by serial FIB sectioning (Fig. 7(i)–(p)). The positions of the simulation results correspond exactly to the cutting positions where the experimental texture mappings were taken. Sections that were more remote from the indent than Section 4 did not reveal a substantial microtexture pattern and are, therefore, not shown. Fig. 8(a) provides a closer view of the microtexture pattern using a different scaling from that in Fig. 7.

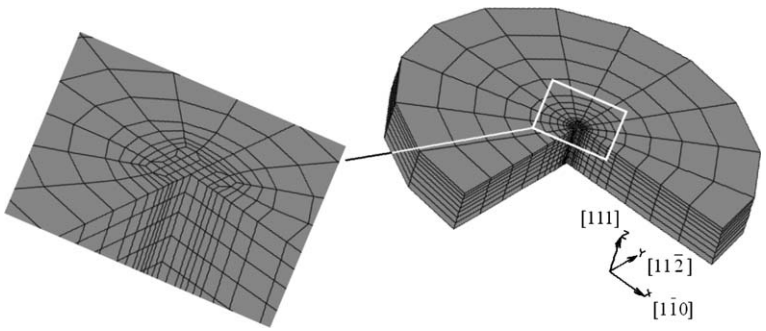

Fig. 4. FEM model. The same mesh was used for the crystal plasticity finite element simulation which considers both elastic and plastic anisotropy and also for the isotropic (J2) finite element simulation. The x, y, z coordinate system represents the $[1\,\bar{1}\,0]$, $[1\,1\,\bar{2}]$, and $[1\,1\,1]$ crystal directions, respectively, in the case of the crystal plasticity finite element simulations.

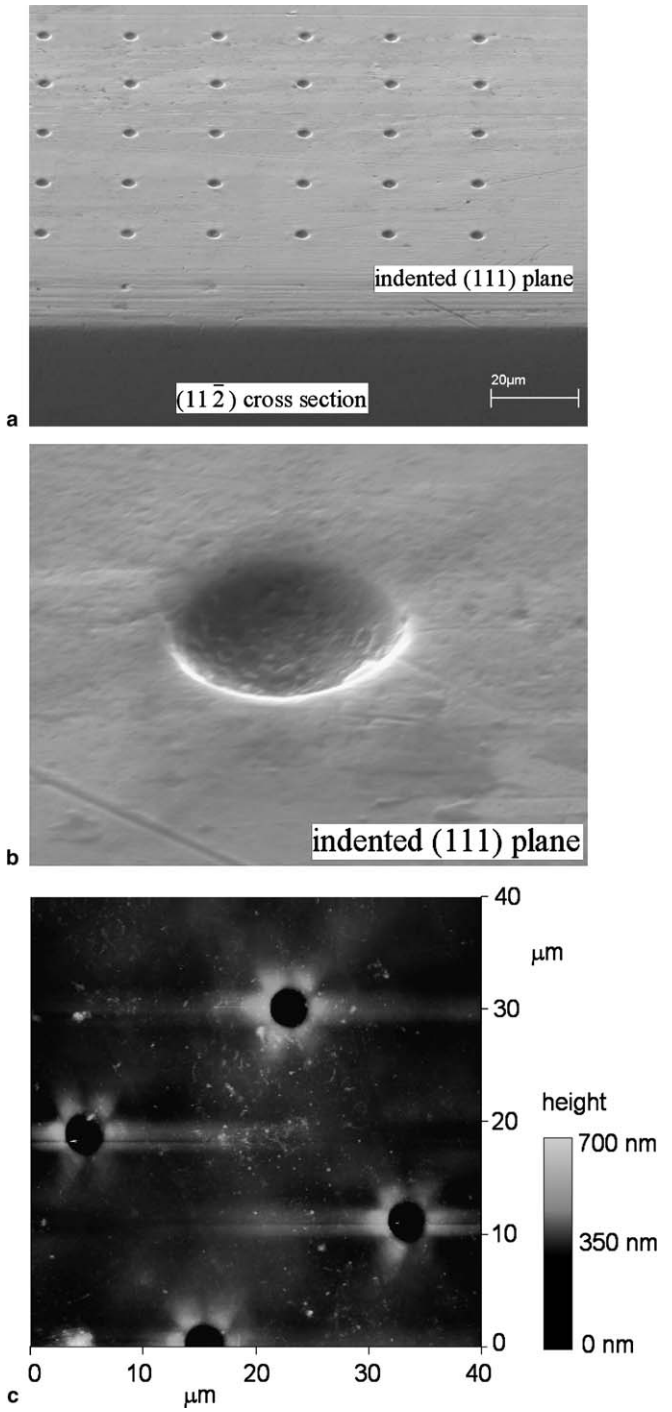

Fig. 5. SEM images of (a) the 6×6 matrix of indents and (b) a close-up of one of the indents. (c) AFM mapping of the surface roughness around the indents in the (1 1 1) plane of the copper single crystal. The AFM image reveals the sixfold pile-up symmetry around the indents characteristic of [1 1 1] indents in Cu [25].

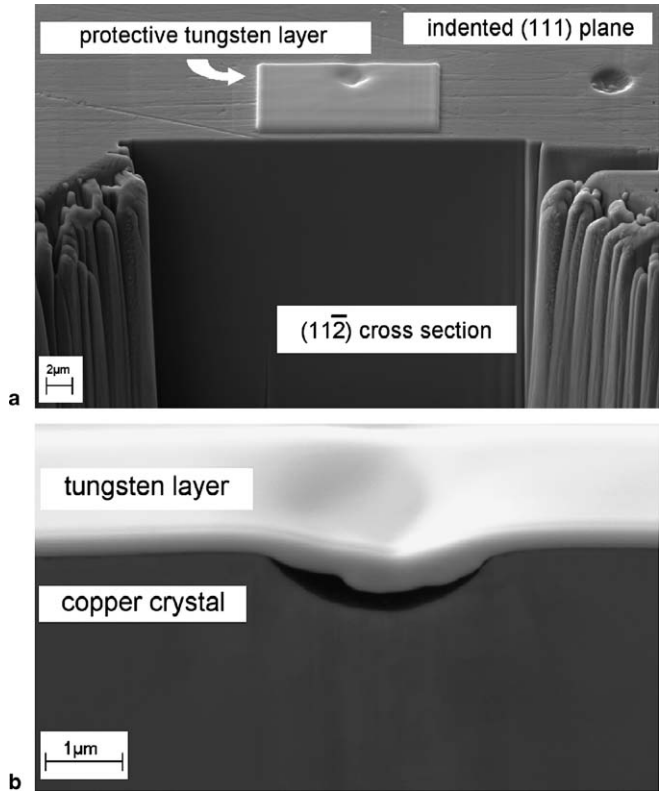

Fig. 6. SEM images of a serial section (a) before the actual indent and (b) at the indent.

One important result from Figs. 7 and 8 is that, although the simulations and experiments show basically similar rotation patterns, they do not reveal a one-to-one correspondence.

The crystal plasticity finite element simulations reveal a single peak behavior for the misorientation pattern in Section 4, i.e., 1567 nm far away from the indenter tip (Fig. 7(a)). In sections closer to the indenter tip (scans 5 and 6; Fig. 7(b) and (c); Table 1) the simulated distribution of the deformation-induced lattice rotations shows a double-well pattern with steep maxima below the zones tangent to the indenter. Sections close to the indenter tip (scans 7–11; Fig. 7(d)–(h)) show a simulated distribution of the lattice rotations with the same dominant double-well pattern with steep reorientation maxima below the tangent zones as already simulated for Sections 5 and 6 but with additional minor rotation zones close to the indenter tip. Of particular interest are the simulation results for scan 7 (Fig. 7(d)) and 11 (Fig. 7(h)). Scan 7 shows a new very small maximum of the deformation-induced rotation in the inner tangent region close to the indenter tip. This pattern can be referred to as an inner double-well pattern (see also the image on the right-hand side of Fig. 9(b)). Scan 11 shows a new maximum in the deformation-induced rotation pattern that appears exactly at the position of the indenter tip. The lateral arrangement of the orientation changes allows one to differentiate coarsely between six different characteristic regions (Fig. 8(b)). Regions 1 and 6 do not reveal large orientation changes (below 4° in the experiment). Regions 2 and 5 are characterized by large strains and correspondingly by large orientation changes (up to 16° in the experiment). Regions 3 and 4 reveal smaller lattice rotations (below 14° in the experiment). The experimental data obtained for scans 6–9 reveal particularly

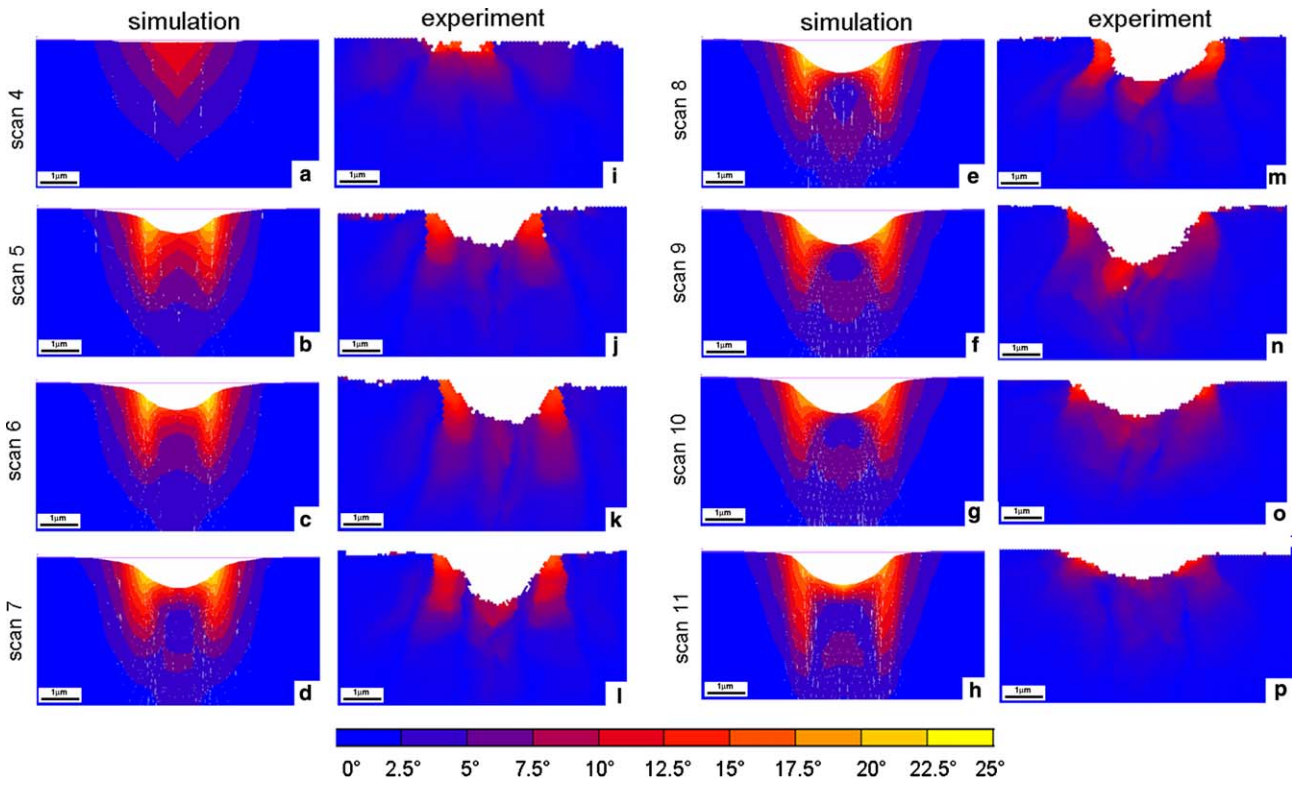

Fig. 7. Rotation maps for a set of successive $(11\bar{2})$ sections perpendicular to the (111) indentation plane (surface plane perpendicular to the plane presented) with different spacing to the actual indent. Scan 4 is far away from the indenter tip (1567 nm) while scan 10 is close to it (176 nm) (see details in Figs. 1 and 2 and Table 1). The images on the left-hand side (a–h) were obtained from viscoplastic crystal plasticity simulations. The corresponding maps on the right-hand side (i–p) were determined via EBSD measurements in succeeding planes prepared by serial FIB sectioning. The color code shows the magnitude of the orientation change relative to the initial crystal orientation without indicating the rotation axis or rotation direction. Scaling is identical for all diagrams.

steep orientation gradients in part over a length of less than 100 nm in the transition area between regions 2 and 3 and regions 4 and 5, respectively (Figs. 7 and 8(a)).

Although showing a similar deformation-induced lattice rotation pattern in terms of the magnitude of the rotations as the simulations (Fig. 7(a)–(h)), the experimental results (Fig. 7(i)–(p)) reveal also some differences. First, the EBSD experiments generally reveal a smaller magnitude of the maximum occurring lattice rotations as compared to the simulations. While the simulations are characterized by

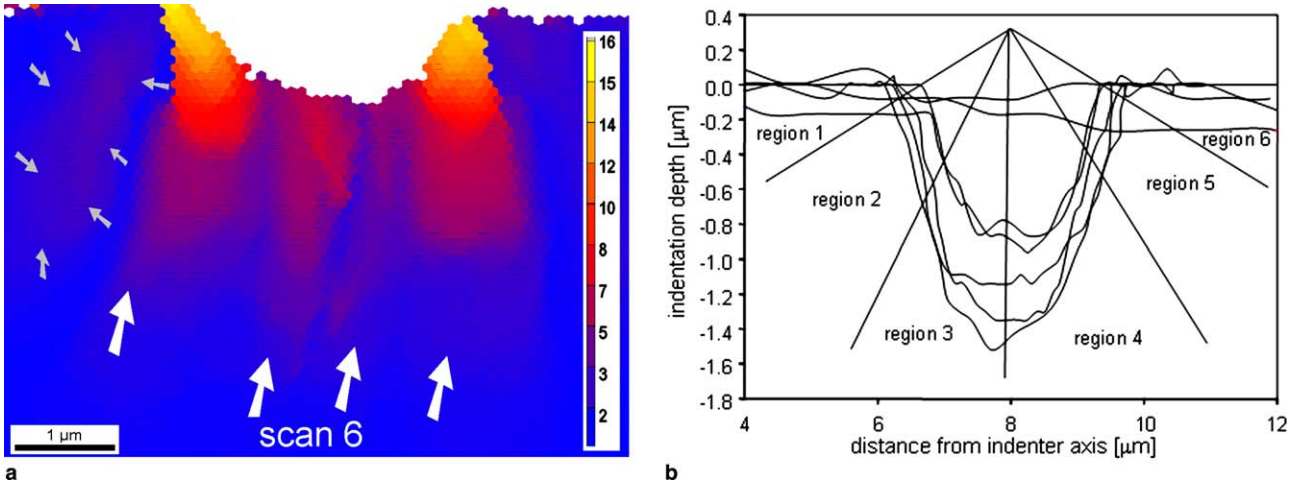

Fig. 8. (a) Closer view of the experimentally observed pattern of the absolute values of the deformation-induced crystalline lattice rotations in degrees in the vicinity of the indent using a different scaling from that in Fig. 7. The rotation axis and rotation direction are not indicated (see Figs. 12–14 for this information). (b) From the distribution of the shear rates and lattice rotations six different deformation zones can be roughly identified. The diagrams are $(11\bar{2})$ sections.

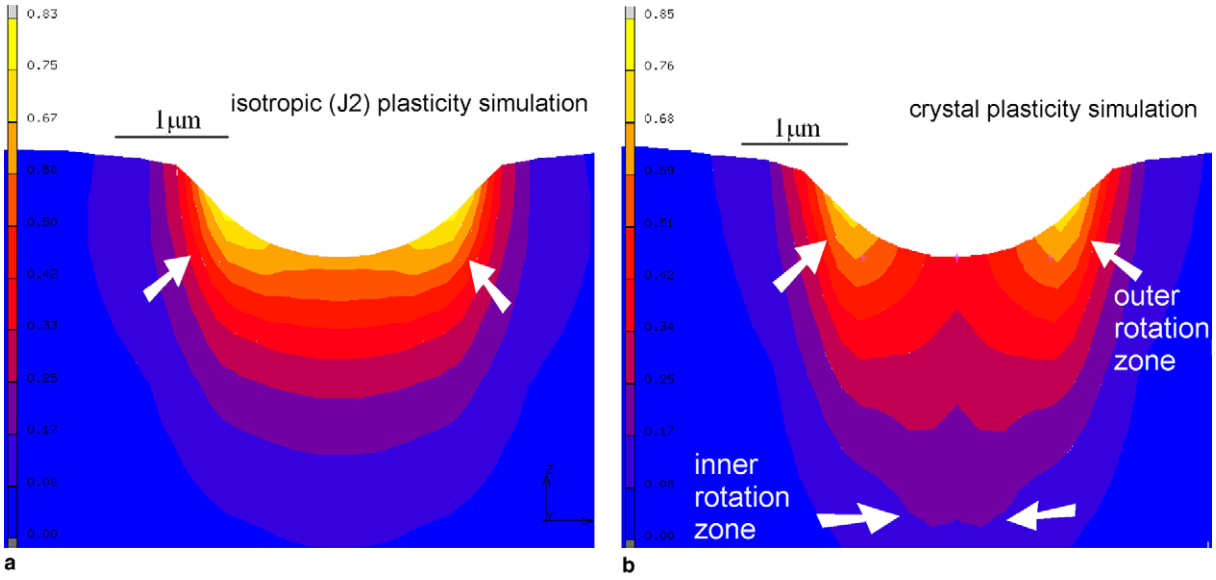

Fig. 9. Von Mises equivalent strain distribution in the middle section directly below the indenter tip obtained from two different types of finite element simulations (same mesh in both cases, see Fig. 4). (a) Finite element simulation with an isotropic plastic constitutive J2 model (no preferred directions; J2: second invariant of the stress deviator as an isotropic yield criterion). (b) Finite element simulation with an anisotropic crystal plasticity constitutive model, as explained in Section 4, in the crystallographic $(1\,1\,\bar{2})$ plane.

maximum misorientations of up to 25° relative to the starting orientation, the experiments show smaller values of the maximum occurring misorientations of only 16°. A second difference between simulation and experiment is that practically all sections obtained from the experiments reveal a pronounced inner pattern (i.e., close to the indenter tip;

Slip Plane	(111)			$(\bar{1}11)$		
Slip Direction	$01\bar{1}$	$\bar{1}01$	$\bar{1}10$	$01\bar{1}$	101	110
Schmid factor	0	0	0	0	0.2722	0.2722
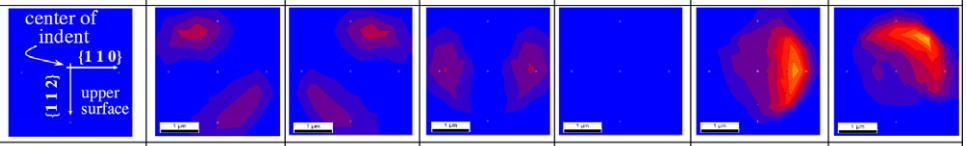						
Shear strain on slip system	0.375	0.376	0.320	0.093	0.740	0.847

Slip Plane	$(1\bar{1}1)$			$(\bar{1}\bar{1}1)$		
Slip Direction	011	$\bar{1}01$	110	011	101	$\bar{1}10$
Schmid factor	0.2722	0	0.2722	0.2722	0.2722	0
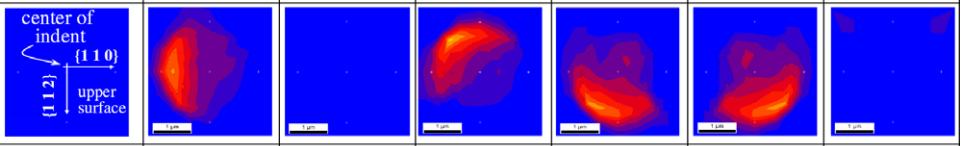						
Shear strain on slip system	0.719	0.094	0.852	0.747	0.754	0.125

Fig. 10. Distribution of the shear strains on all 12 slip systems as extracted from the crystal plasticity finite element simulation in the indented (1 1 1) plane. Six systems carry the largest portion of the deformation (the amount of shear is given in the bottom rows). The Schmid factors are calculated for the simplified assumption of compression along the [1 1 1] axis.

see white arrows in Fig. 8(a)) of orientation changes within the larger outer double-well pattern tangent to the indent that dominated the predicted rotation pattern. In general it seems that the experimentally observed rotation patterns are characterized by a more rapid change in the rotation field among neighboring material portions than the simulations. This point will be discussed below in more detail when analyzing also the direction of the deformation-induced rotations. A third obvious difference between simulation and experiment is that the experimental data are less symmetric than the predicted ones since the experimentally observed rotation patterns appear somewhat distorted at least in some sections.

Concerning the deviation in the magnitude of the simulated and experimentally observed orientation changes, two aspects have to be considered. The first is that owing to edge effects and milling-induced curvature, the EBSD method misses mapping the microstructure that is closest to the actual interface between the indented material and the surface of the indenter. These zones are the ones where the rotation rates should be highest according to the simulated deformation and rotation patterns. This means that the interface layers with the largest deformation-induced rotations were probably not completely mapped by the experiment. This might amount to a layer of 100–200 nm at most and would explain the difference in the magnitude of the rotations observed between the experiment and simulation. The second aspect is the fact that the crystal plasticity finite element simulation method used in the current work does not take into account gradient terms at a slip system level in the constitutive description. This means that the predicted rotation rates are presumably exaggerated. The reason for this assumption is that the consideration of gradient terms in a crystal plasticity constitutive environment exerts a penalty term against high local rotation rates of the lattice. This applies in particular when neighboring material portions have less of a tendency to follow that rotation. In such a case (which is typical of an indentation boundary condition) such rapid changes in the local texture evolution require a rapid corresponding accumulation of geometrically necessary dislocations for the accommodation of the resulting mismatch in the lattice spin among neighboring material portions [20–24,41–45]. The observation that the experimentally observed rotation patterns show at least four (if not more, see faint maximum on the left-hand side of Fig. 8(a), small gray arrows) characteristic misorientation peaks much more clearly than the simulations can be discussed in terms of Fig. 9. This figure shows the von Mises equivalent strain distribution in the middle section directly below the indenter tip as obtained from two different types of finite element simulations. The simulation result in Fig. 9(a) shows finite element simulations with an isotropic plastic constitutive model without any preferred crystallographic directions. The result in Fig. 9(b) shows simulations with the anisotropic crystal plasticity constitutive model as introduced above ($(11\bar{2})$ section). Both types of simulations were conducted using the same mesh (Fig. 4). The comparison between the isotropic and the anisotropic case clearly reveals that the main outer double-well pattern where the deformation (and hence also the crystalline rotation) is accumulated in the shear zones tangent to the indent is not a purely crystalline phenomenon but occurs also in the isotropic case (see arrows in Fig. 9(a)). The crystal plasticity simulation shows the same outer double-well strain pattern as the isotropic simulation, but it reveals additionally a second inner double-well pattern (see arrows at the bottom of Fig. 9(b)). This means that the inner portion of the strain pattern, which supposedly gives rise to a corresponding rotation pattern (Figs. 7 and 8) has a clearly crystallographic origin, i.e., it must be due to the crystalline discreteness of the plastic slip.

Fig. 10 provides a more detailed view of the simulated distribution of the plastic deformation around the indent. It reveals for each of the 12 slip systems the accumulated

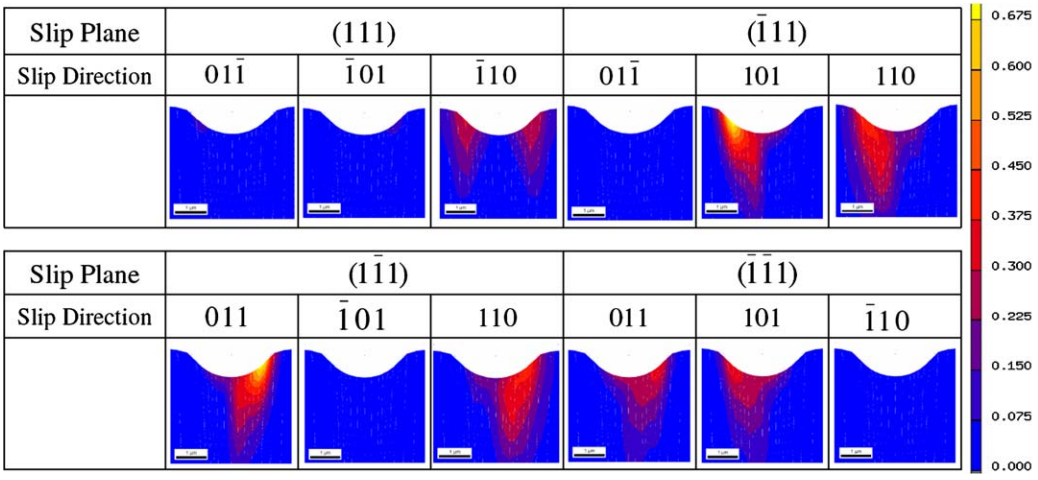

Fig. 11. Distribution of the shear strains on the 12 slip systems, predicted by the crystal plasticity finite element simulation. View in the crystallographic $(11\bar{2})$ plane below the indenter tip.

shear strain as predicted by the crystal plasticity finite element simulation. The result shows that six slip systems carry the largest portion of the overall plastic deformation (see the amount of shear in the two bottom rows). These dominant systems are the$(\bar{1}\,1\,1)[1\,0\,1]$, $(\bar{1}\,1\,1)[1\,1\,0]$, $(1\,\bar{1}\,1)[0\,1\,1]$, $(1\,\bar{1}\,1)[1\,1\,0]$, $(\bar{1}\,\bar{1}\,1)[0\,1\,1]$, and $(\bar{1}\,\bar{1}\,1)[1\,0\,1]$ slip systems. This result of the simulation is quite obvious and matches earlier observations [25]. It is in accord with the maximum orientation factors on these systems for the simplified assumption of compression along the [1 1 1] axis. The result also matches and explains the sixfold symmetric pile-up pattern faintly visible in Fig. 5(b) (SEM) and more clearly in Fig. 5(c) (AFM) around the indent.

It is worth noting that a second set of slip systems pertaining to the indented (1 1 1) plane, namely $(1\,1\,1)[0\bar{1}\,1]$, $(1\,1\,1)[\bar{1}\,0\,1]$, and $(1\,1\,1)[\bar{1}\,1\,0]$, also contribute significantly to the total deformation when compared to the strain provided by the six dominant systems listed above. The fact that the orientation factors of these slip systems are zero in the table is of course due to the simplifying assumption of uniaxial compression that was made to calculate them. The amounts of shear listed in the table, in contrast, stem from the actual crystal plasticity finite element simulation, which imposes the correct boundary conditions locally. One special feature of this second group of slip systems is the high symmetry of the shear they contribute (two peaks of shear are visible on either side of the indenter axis).

Fig. 11 shows the distribution of the shear strains on all 12 slip systems as extracted from the crystal plasticity finite element simulation in the crystallographic $(1\,1\,\bar{2})$ plane. As already observed from the top view in the (1 1 1) plane in Fig. 10, the dominant slip systems that essentially carry the strain in the $(1\,1\,\bar{2})$ plane are the $(\bar{1}\,1\,1)[1\,0\,1]$, $(\bar{1}\,1\,1)[1\,1\,0]$, $(1\,\bar{1}\,1)[0\,1\,1]$, $(1\,\bar{1}\,1)[1\,1\,0]$, $(\bar{1}\,\bar{1}\,1)[0\,1\,1]$, and $(\bar{1}\,\bar{1}\,1)[1\,0\,1]$ systems. Minor shear activity can be observed on the $(1\,1\,1)[\bar{1}\,1\,0]$ slip system. An equivalent shear contribution on two other systems, $(1\,1\,1)[0\bar{1}\,1]$ and $(1\,1\,1)[\bar{1}\,0\,1]$, also exists with a similar pattern as observed for the $(1\,1\,1)[\bar{1}\,1\,0]$ slip system, but it cannot be seen in this crystallographic section (see the same systems also in Fig. 10). The shear distribution on the main slip systems$(\bar{1}\,1\,1)[1\,0\,1]$, $(\bar{1}\,1\,1)[1\,1\,0]$, $(1\,\bar{1}\,1)[0\,1\,1]$, $(1\,\bar{1}\,1)[1\,1\,0]$, $(\bar{1}\,\bar{1}\,1)[0\,1\,1]$, and $(\bar{1}\,\bar{1}\,1)[1\,0\,1]$ prevails also in the deeper regions far below the indenter tip where a change in the rotation sign was observed (Figs. 7 and 8).

The subdivision of the deformation pattern into six different characteristic regions suggested as a coarse subdivision in Fig. 8 is also helpful for discussing the sense and axis of the deformation-induced lattice rotations. Fig. 12 shows the lattice rotations about the crystallographic $[1\,\bar{1}\,0]$ axis presented in the $(1\,1\,\bar{2})$ plane (Fig. 12(a)) and in the $(1\bar{1}0)$ plane (Fig. 12(b)) as predicted by the crystal plasticity finite element simulation. Both figures reveal the same rotation pattern as observed above, but they include the rotation direction. They both show one outer pair of zones with large lattice rotations tangent to the

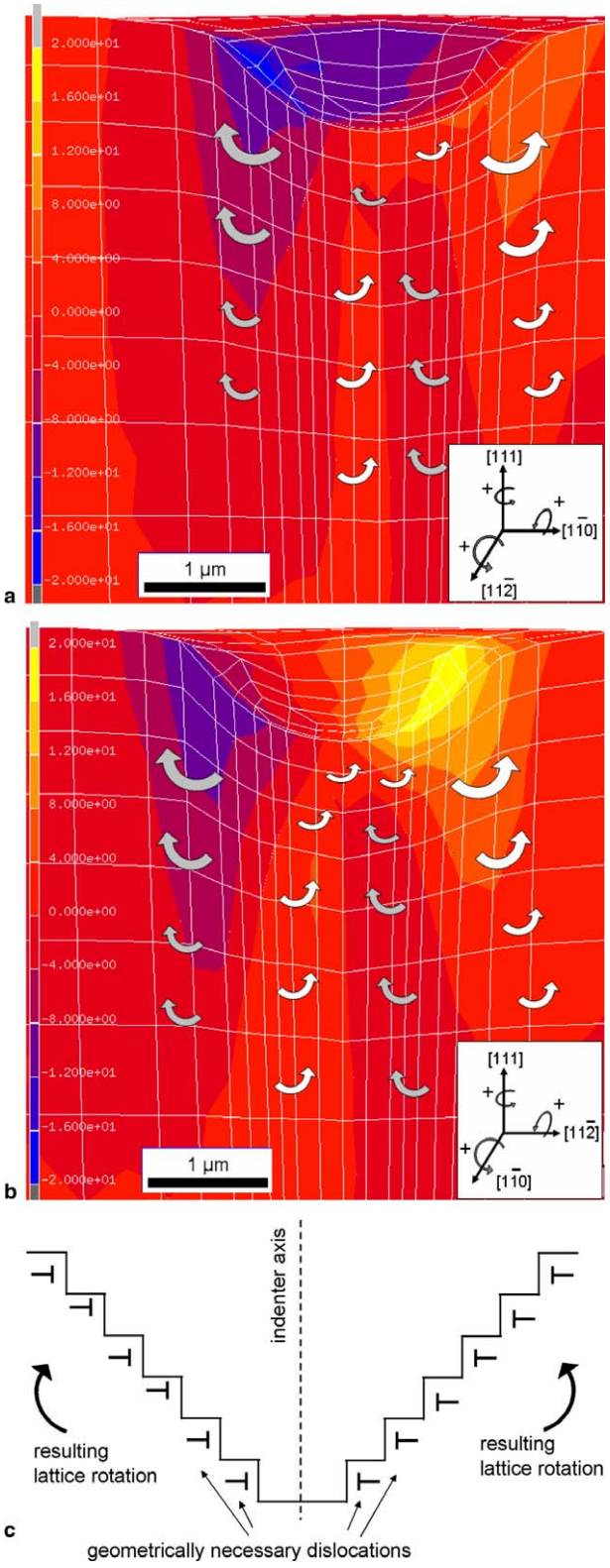

Fig. 12. 3D presentation of the simulated rotations (crystal plasticity finite element model) about the crystallographic $[1\,\bar{1}\,0]$ axis presented (a) in the $(1\,1\,\bar{2})$ plane and (b) in the $(1\,\bar{1}\,0)$ plane. The planes presented are center planes, i.e., they both contain the indenter axis as a common zone axis. Scaling is the same for (a) and (b), i.e., from −20° to +20°. (c) Schematic of the arrangement of the net geometrically necessary dislocations explaining the rotation direction in the outer tangent zones.

indenter surface and a second inner pair of zones with smaller lattice rotations close to the tip of the indenter. Different from the images discussed above which only revealed the absolute amount of the rotations, the simulation results in Fig. 12 show that in the tangent regime the $[1\,\bar{1}\,0]$ rotations point away from the indenter axis while in the inner zone the rotations point towards the indenter tip. This means that a transition regime exists between the outer and the inner deformation zone that is characterized by steep gradients and, in particular, by a change in the sign of the rotation direction.

The predicted profile with large rotations in the tangent zones (regions 2 and 5; large symbols in Fig. 12(a) and (b)) can be qualitatively understood in terms of the mass that must be displaced by the indenter from the bulk towards the surface. This large-scale displacement naturally creates the rotation angle confirmed by the 3D EBSD measurements (Fig. 13) and by the crystal plasticity simulations (Fig. 12). Another more detailed picture matching this tangent rotation field is the pattern of the net amount of geometrically necessary dislocations that has to be created for compatibility reasons in the tangent zones (Fig. 12(c)). Although both approaches allow one to reconstruct basically the induced rotation pattern in the outer tangent zones (regions 2 and 5), the counter-rotations observed in the inner deformation zone close to the indenter axis are not a necessary consequence of this explanation.

Fig. 13 shows the rotation angles and the rotation directions in the $(1\,1\,\bar{2})$ plane in scan 9 (see details in Table 1). This $(1\,1\,\bar{2})$ section is placed 318 nm before the actual indenter tip. The upper row shows the rotations in that plane for the $[1\,\bar{1}\,0]$ rotation axis. The image on the left-hand side shows the $[1\,\bar{1}\,0]$ rotations scaled to $\pm 8°$. The center image shows the same data scaled to $\pm 20°$ for better comparison with the crystal plasticity finite element simulations on the right-hand side in the same row. The images in the bottom row show the rotations in the $(11\bar{2})$ plane in scan 9, but for the $[1\,1\,\bar{2}]$ rotation axis. The image on the left-hand side shows the $[1\,1\,\bar{2}]$ rotations scaled to $\pm 8°$. The center image shows the same data scaled to $\pm 20°$ for comparison with the simulations on the right-hand side in the same row.

The experimental maps of the rotation directions about the $[1\,\bar{1}\,0]$ and $[1\,1\,\bar{2}]$ rotation axes (images on the left-hand

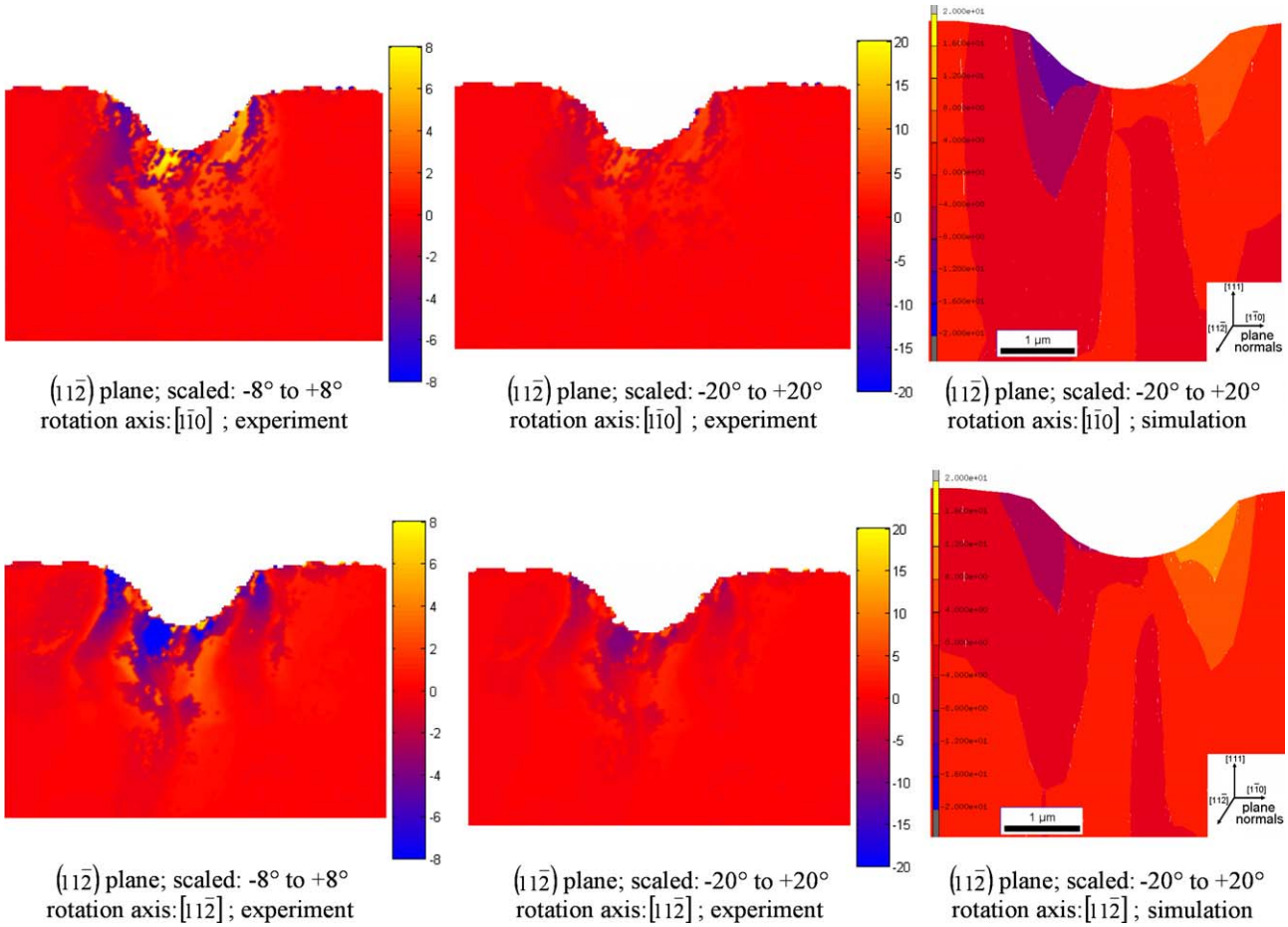

Fig. 13. Rotation angles and rotation directions in the $(1\,1\,\bar{2})$ plane for scan 9 (see Table 1). This $(1\,1\,\bar{2})$ section is 318 nm before the indenter tip. Top row: rotations in the $(1\,1\,\bar{2})$ plane for the $[1\,\bar{1}\,0]$ rotation axis; left: $[1\,\bar{1}\,0]$ rotations scaled to $\pm 8°$; center: same data scaled to $\pm 20°$ for better comparison with the simulations; right: $[1\,\bar{1}\,0]$ rotations from crystal plasticity finite element simulations scaled to $\pm 20°$. Bottom row: rotations in the $(1\,1\,\bar{2})$ plane for the $[1\,1\,\bar{2}]$ rotation axis; left: $[1\,1\,\bar{2}]$ rotations scaled to $\pm 8°$; center: same data scaled to $\pm 20°$ for better comparison with the simulations; right: $[1\,1\,\bar{2}]$ rotations from crystal plasticity finite element simulations scaled to $\pm 20°$.

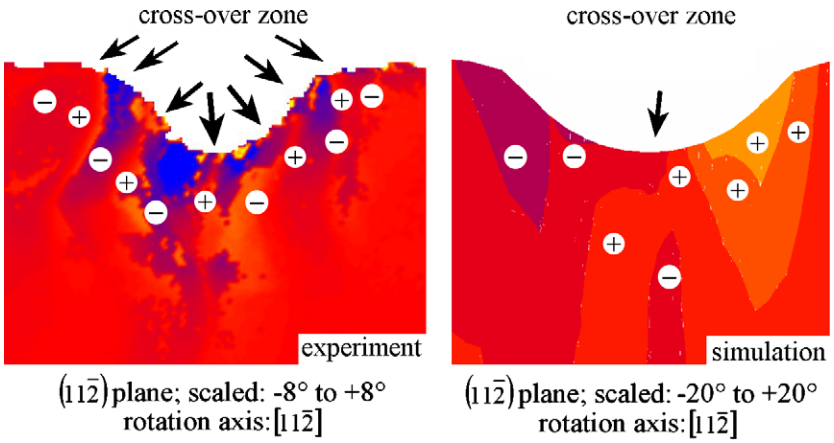

Fig. 14. Detail from Fig. 13 (bottom row; $[1\,1\,\bar{2}]$ rotations in $(1\,1\,\bar{2})$). The experimentally observed rotation pattern reveals a larger number of cross-over zones, where the sign of the rotation direction changes, when compared to the simulated results (note the difference in scaling). The signs indicate positive or negative rotation direction about the $[1\,1\,\bar{2}]$ axis.

side in Fig. 13) basically show a similar deformation-induced rotation pattern as discussed above in the context of the absolute values of the deformation-induced rotations (Figs. 7–9). Also the experimentally observed patterns of the rotation directions reveal some basic similarities to those predicted by the crystal plasticity finite element method (images on the right-hand side in Fig. 13).

The possible reason for differences in the absolute magnitude of the rotation angles has been discussed above in terms of rim and edge effects. Besides this discrepancy, another main difference in the rotation direction field between experiment and simulation is that the experiments reveal a larger number of changes in the sign of the rotation direction along the contact zone between sample and indenter. This applies to both $[1\,\bar{1}\,0]$ and $[1\,1\,\bar{2}]$ rotation axes. The difference is particularly apparent in the map of the $[1\,1\,\bar{2}]$ rotations in the $(1\,1\,\bar{2})$ plane scaled to $\pm 8°$ (Fig. 13, bottom row, left). Fig. 14 shows a detail from Fig. 13 (bottom row; $[1\,1\,\bar{2}]$ rotations in $(1\,1\,\bar{2})$), which reveals that the experimentally observed rotation pattern shows a higher number of cross-over zones, where the sign of the rotation direction changes, when compared to the simulated results.

This applies in particular to the rapid changes in the sign of the rotation direction along the outer tangent zones. In these areas far away from the indenter tip the predicted rotation pattern also reveals gradients in the orientation field, but no frequent switches in sign are observed as in the experiments. This comparison shows that the viscoplastic crystal plasticity finite element simulation of nanoindentation presented in this work is obviously not capable of capturing the fine details of the deformation-induced rotation patterning observed in the experiment, at least not when it comes to the direction of rotation. The results shown in Fig. 9 (comparison of the equivalent strain field obtained from an isotropic simulation and from an anisotropic simulation) emphasize that the details of the deformation field must indeed be linked to crystallographic aspects. Therefore, one may hope to obtain better simulation results with regard to steep gradients in the rotation field by incorporating more detailed constitutive descriptions in the crystal plasticity finite element model. Owing to our experimental data these model variants should in particular include two aspects. These are (i) gradient effects at the single slip level and (ii) dislocation patterning effects. The first aspect is obvious owing to the gradient mechanics associated with nanoindentation [8–11]. The second aspect seems to be of relevance because we assume that the pronounced patterning of the deformation-induced rotation field both in terms of the absolute orientation changes (e.g., Figs. 7 and 8) and of the rotation direction (Figs. 12–14) can only be fully understood by taking into account short-range dislocation patterning aspects, which would impede the formation of the smooth rotation fields predicted by our current simulations.

6. Conclusions

We have presented a 3D analysis of the deformation-induced rotation pattern below a conical nanoindent in a $[1\,1\,1]$ Cu single crystal using a 3D EBSD experimental method and a 3D elastic–viscoplastic crystal plasticity finite element method for the simulations. The main conclusions are as follows.

- A new microscopy approach using a combined SEM/FIB was for the first time applied to the 3D EBSD analysis of nanoindentation. Particular attention was placed on studying deformation-induced lattice rotations.
- The experiments and simulations reveal pronounced deformation-induced 3D patterning of the lattice rotations below and around the indent.
- The simulated pattern is characterized by an outer tangent zone with large rotations and an inner zone closer to the indenter axis with smaller rotations. The rotations in the tangent regime point away from the indenter axis

while in the inner zone the rotations point towards the indenter tip. This leads to a transition regime between the outer and the inner rotation zone that is characterized by steep orientation gradients and a change in the sign of the rotation direction (cross-over zone).

- The experimentally observed pattern is characterized by similar features in the overall rotation distribution to the simulations. In particular, the crystal plasticity finite element simulations reveal a similar pattern formation in terms of the absolute rotation rates as the experiments. However, when analyzing details of the axis–angle relationship of the rotations the experiments clearly reveal a higher frequency of cross-over zones, where the sign of the rotation direction changes, than the simulations. Some of these cross-over zones are not captured at all by the simulations.
- The crystal plasticity finite element simulations provide details of the shear distribution in the deformation zone on the different slip systems. The main shear contribution is carried by those six slip systems that would also be expected from a maximum orientation factor analysis for the simplifying case of uniaxial compression along $\langle 1\,1\,1\rangle$.
- The isotropic (J2 flow criterion) finite element simulations only reveal an outer pronounced deformation zone, but the inner deformation zone is not predicted, which underlines its crystallographic origin. This observation emphasizes that corresponding simulations of nanoindentation must take the crystallographic nature of the plastic slip into account.

Acknowledgements

We gratefully acknowledge the kind financial support of the Deutscher Akademischer Austauschdienst (DAAD, German Academic Exchange Service; www.daad.org) for N.Z. and of the Alexander von Humboldt Stiftung (AvH, Alexander von Humboldt Foundation, www.humboldt-foundation.de) for R.N.S. The authors are also grateful to the Deutsche Forschungsgemeinschaft (DFG, German Research Foundation, www.dfg.de), which funded this study under the framework of the Gottfried Wilhelm Leibniz award. Detailed discussions on this topic during the last two years with Dr. Ben Larson and Dr. Wenge Yang from the Oak Ridge National Laboratory, USA, are gratefully acknowledged.

References

[1] Pharr GM, Oliver WC, Brotzen FR. J Mater Res 1992;7:613–7.
[2] Oliver WC, Pharr GM. J Mater Res 1992;7:1564–83.
[3] Fischer-Cripps AC. Nanoindentation. Springer mechanical engineering series. 2nd ed. Berlin: Springer; 2004.
[4] Nix WD. Mater Sci Eng A 1997;234–236:37–44.
[5] Choi Y, Van Vliet KJ, Li J, Suresh S. J Appl Phys 2003;94:6050–8.
[6] Suresh S, Giannakopolous AE. Acta Mater 1998;46:5755–67.
[7] Gouldstone A, Koh H-J, Zeng K-Y, Giannakopoulos AE, Suresh S. Acta Mater 2000;48:2277–95.
[8] Fleck NA, Muller GM, Ashby MF, Hutchinson JW. Acta Metall Mater 1994;42:475–87.
[9] Fleck NA, Otoyo H, Needleman A. Int J Solids Struct 1992;26:1613–36.
[10] Gao H, Huang Y, Nix WD, Hutchinson JW. J Mech Phys Solids 1999;47:1239–636.
[11] Evers LP, Parks DM, Brekelmans WAM, Geers MGD. J Mech Phys Solids 2002;50:2403–24.
[12] Viswanathan GB, Lee E, Maher DM, Banerjee S, Fraser HL. Acta Mater 2005;53:5101–15.
[13] Groeber M, Haley B, Uchic M, Ghosh S. In: Ghosh S, Castro J, Lee JK, editors. Proceedings of NUMIFORM. AIP Publishers; 2004. p. 1712.
[14] Zaefferer S. Mater Sci Forum 2005;495–497:3–12.
[15] Konrad J, Zaefferer S, Raabe D. Acta Mater 2006; in press.
[16] Raabe D, Klose P, Engl B, Imlau KP, Friedel F, Roters F. Adv Eng Mater 2002;4:169–80.
[17] Raabe D, Roters F. Int J Plasticity 2004;20:339–61.
[18] Raabe D, Sachtleber M, Zhao Z, Roters F, Zaefferer S. Acta Mater 2001;49:3433–41.
[19] Sachtleber M, Zhao Z, Raabe D. Mater Sci Eng A 2002;336:81–7.
[20] Yang W, Larson BC, Pharr GM, Ice GE, Tischler JZ. MRS Symp Proc 2003;779:W5.34.1.
[21] Larson BC, Yang W, Ice GE, Budai JD, Tischler JZ. Nature 2002;415:887–90.
[22] Barabash RI, Ice GE, Larson BC, Pharr GM, Chung KS, Yang W. Appl Phys Lett 2001;79:749.
[23] Ice GE, Larson BC. Adv Eng Mater 2000;2:643.
[24] Larson BC, personal communication and lectures at the Plasticity 2005 conference in Kauai (Hawaii, USA) and at the MRS 2005 spring conference in San Francisco.
[25] Wang Y, Raabe D, Klüber C, Roters F. Acta Mater 2004;52:2229–38.
[26] Shilkrot LE, Curtin WA, Miller RE. J Mech Phys Solids 2002;50:2085–2106.
[27] Miller RE, Shilkrot LE, Curtin WA. Acta Mater 2004;52:271–84.
[28] Smith GS, Tadmor EB, Bernstein N, Kaxiras E. Acta Mater 2001;49:4089–101.
[29] Bolshakov A, Pharr GM. J Mater Res 1998;13:1049–58.
[30] Fivel MC, Robertson CF, Canova GR, Boulanger L. Acta Mater 1998;46:6183–94.
[31] Durst K, Göken M, Pharr GM. Z Metallkd 2002;93:857–61.
[32] Park YJ, Pharr GM. Thin Solid Films 2004;447:246–50.
[33] Lichinchi M, Lenardi C, Haupt J, Vitali R. Thin Solid Films 1998;312:240–8.
[34] Durst K, Backes B, Göken M. Scripta Mater 2005;52:1093–7.
[35] Durst K, Göken M, Vehoff H. J Mater Res 2004;19:85–93.
[36] Li J, Van Vliet K, Ting Z, Yip S, Suresh S. Nature 2002;418:307–310.
[37] Van Vliet K, Li J, Ting Z, Yip S, Suresh S. Phys Rev B 2003;67:104105.
[38] Kalidindi SR, Bronkhorst CA, Anand L. J Mech Phys Solids 1992;40:537–69.
[39] Kalidindi SR, Anand L. Metall Trans A 1993;24:989–92.
[40] MSC. Marc user manual, vol. D. MSC Software Corporation; 2001.
[41] Ma A, Roters F, Raabe D. Acta Mater 2006; in press.
[42] Raabe D, Zhao Z, Park SJ, Roters F. Acta Mater 2002;50:421–40.
[43] Meissonnier FT, Busso EP, O'Dowd NP. Int J Plasticity 2001;17:601–40.
[44] Arsenlis A, Parks DM, Becker R, Bulatov V. J Mech Phys Solids 2004;52:1213–46.
[45] Evers LP, Brekelmans WAM, Geers MGD. J Mech Phys Solids 2004;52:2379–401.